An Improved Modeling for Low-grade Organic Rankine Cycle Coupled with Optimization Design of Radial-inflow Turbine

Lijing Zhai[a], Guoqiang Xu[a], Jie Wen[a,*], Yongkai Quan[a], Jian Fu[a],

Hongwei Wu[b,**], Tingting Li[c],

[a] National Key Laboratory of Science and Technology on Aero-Engine Aero-thermodynamics, School of Energy and Power Engineering, Beihang University, Beijing 100191, China

[b] School of Engineering and Technology, University of Hertfordshire, Hatfield, AL10 9AB,United Kingdom

[c] Department of Mechanical Engineering, Texas A&M University, College Station, TX77843-3123, United States

* Corresponding author.   Email: wenjie@buaa.edu.cn   Tel. +86(010)82338335

** Corresponding author.   Email: h.wu6@herts.ac.uk

23 **Abstract**

24   Organic Rankine cycle (ORC) has been proven to be an effective and promising

25 technology to convert low-grade heat energy into power, attracting rapidly growing

26 interest in recent years. As the key component of the ORC system, turbine

27 significantly influences the overall cycle performance and its efficiency also varies

28 with different working fluids as well as in different operating conditions. However,

29 turbine efficiency is generally assumed to be constant in the conventional cycle design.

30 Aiming at this issue, this paper couples the ORC system design with the radial-inflow

31 turbine design to investigate the thermodynamic performance of the ORC system and

32 the aerodynamic characteristics of radial-inflow turbine simultaneously. The

33 constrained genetic algorithm (GA) is used to optimize the radial-inflow turbine with

34 attention to six design parameters, including degree of reaction, velocity ratio, loading

35 coefficient, flow coefficient, ratio of wheel diameter, and rotational speed. The

36 influence of heat source outlet temperature on the performance of the radial-inflow

37 turbine and the ORC system with constant mass flow rate of the heat source and

38 constant heat source inlet temperature is investigated for four kinds of working fluids.

39 The net electrical powers achieved are from few tens kWs to one hundred kWs. The

40 results show that the turbine efficiency decreases with increasing heat source outlet

41 temperature and that the decreasing rate of turbine efficiency becomes faster in the

42 high temperature region. The optimized turbine efficiency varies from 88.06% (using

43 pentane at the outlet temperature of 105 ℃) to 91.01% (using R245fa at the outlet

44 temperature of 80 ℃), which appears much higher compared to common values

45 reported in the literature. Furthermore, the cycle efficiency increases monotonously

46 with the growth of the heat source outlet temperature, whereas the net power output

47 has the opposite trend. R123 achieves the maximum cycle efficiency of 12.21% at the

48 heat source outlet temperature of 110 ℃. Based on the optimized results, the

49 recommended ranges of the key design parameters for ORC radial-inflow turbine are

50 presented as well.

51 **Keywords**

52 Organic Rankine cycle; Radial-inflow turbine; Coupled modeling; Genetic algorithm

53

54

55

56

57

58

59

60

61

62

63

64

65

66

67

68

69

1. Introduction

Nowadays, with rapidly increasing globalization and energy demands, researchers are devoted to solving problems of energy shortage and environmental pollution. Apart from the development of new energy sources, the recovery and utilization of renewable energy, such as solar energy [1-3], biomass energy [4, 5], geothermal energy [6-9] and waste heat [10-12], have attracted increasing attention. Because of the advantages of low capital cost, small size and easy maintenance [13], Organic Rankine cycle (ORC), which has the same configuration as conventional steam Rankine cycle but uses organic fluid instead of water as working fluid, has been proved to be an effective and promising technology for the low-grade heat recovery.

Over the past two decades, a large part of relevant research studies focuses on the working fluid selection. Dry and isentropic fluids with positive slopes or infinitely large slopes of vapor saturation curves in the temperature-entropy diagram are preferable due to their convenience in the non-superheating ORC [14]. Additionally, a suitable working fluid should also satisfy cycle and turbine performances, safety and environmental criteria [15]. Wang et al. [16] evaluated R11, R141b, R123, R245fa and R245ca as working fluids for engine waste heat recovery. R245fa and R245ca were recommended as the most suitable working fluids for an engine waste heat-recovery application. Rayegan and Tao [17] developed a procedure to compare 117 organic fluids in solar ORC. R245fa and R245ca were selected for the medium temperature level. Drescher and Bruggemann [18] investigated suitable working fluids for ORC in biomass power plants. It was found that the family of alkylbenzenes showed the highest cycle efficiencies. Qiu [19] proposed a preferable ranking of 8 mostly-applied working fluids by means of spinal point method in micro-CHP (combined heat and power) systems. In general, the selection of working fluids is a complex process,

95 which is affected by the heat source type and level, operating conditions, cycle

96 configuration, the turbine types and performance. The results of working fluid

97 selection do not have universality because of widely varying cycle operation

98 conditions, diverse cycle configurations, different aims for working fluid selection in

99 terms of different application background and so forth [20].

100 It is also noted that determination and optimization of the ORC system

101 parameters are another hot topic in the field of ORC. Peris et al. [21] studied the

102 performance of a regenerative ORC with heat source inlet temperature of 127-156 ℃

103 experimentally. The inlet pressure of volumetric expander was about 14-20 bar and

104 the maximum electrical efficiency of 12.32% was obtained at the heat source inlet

105 temperature of 155 ℃. Braimakis and Karellas [22] presented an integrated

106 thermoeconomic optimization approach of standard and regenerative ORCs. It was

107 concluded that for small scale ORCs the most important costs were related to heat

108 exchangers and the pump while for large scale ORCs screw expanders and turbines

109 were preferred and they had very high costs. Mehrpooya and Ashouri [23] performed

110 a thermoeconomic analysis of a regenerative two-stage ORC with solar energy as heat

111 source to minimize the product cost and maximize the exergy efficiency. The cycle

112 efficiency of 19.59% was reached and product cost rate was 3.88 million dollars per

113 year. Yang and Yeh [24] analyzed the ORC system for geothermal application with

114 heat source inlet temperature of 100 ℃ and mass flow rate of 80 kg/s and found that

115 the higher the operating pressures were, the larger the proportion of purchased cost

116 would be. Marion et al. [25] conducted theoretical and experimental studies on a solar

117 subcritical ORC and concluded that the net mechanical power strongly depended on

118 the fluid mass flow rate and that the optimum mass flow rate was a linear function of

119 the solar radiation. Apart from the standard ORC system, advanced ORC systems like

120   recuperative ORC [26, 27], regenerative ORC [22, 28], supercritical ORC [29-31],

121   zeotropic ORC [32, 33] and trilateral cycle [34, 35] also have been studied

122   extensively.

123   The turbine design is a critical step in the design of ORC systems since turbine

124   geometry and aerodynamic performance directly affect the overall cycle performance

125   and vice versa. Among kinds of ORC expanders, the radial-inflow turbine shows good

126   aerodynamic performance due to its capability of dealing with large enthalpy drops

127   with relatively low peripheral speeds [36]. The conventional turbine design method

128   used for gas turbine is also applicable to the design of an ORC turbine. Due to the

129   lack of extensive experimental data, the loss models are often based on the

130   experimental studies of gas turbine. Fiaschi et al. [36] discussed a 0-D model for the

131   design of radial turbine for 50 kW ORC applications and investigated the estimation

132   of the turbine losses and the main design parameters. The total-to-total efficiency of

133   the designed turbine ranged from 0.72 to 0.80 and backswept bladed rotors showed

134   1.5-2.5% higher efficiencies. Song et al. [37] proposed a 1-D aerodynamic analysis

135   model of the radial-inflow turbine and a performance prediction model of the heat

136   exchanger. The expansion ratio of the six working fluids in the radial-inflow turbine

137   was about 5-25 when the evaporation temperature was 360-430 K. Sauret and Gu [38]

138   performed preliminary steady-state 3-D computational fluid dynamics (CFD)

139   simulations of radial turbine for a number of operating conditions. The maximum

140   turbine efficiency was 88.45% with rotational speed of 25463.5 rpm and turbine inlet

141   temperature of 413 K. Kang [39] examined a two-stage radial turbine with the

142   expansion ratio of the high-pressure turbine as 2.67 and the expansion ratio of the

143   low-pressure turbine as 4.07. The maximum electric power, average cycle and turbine

144   efficiencies were found to be 39.0 kW, 9.8% and 58.4% when the evaporation

145   temperature was 116 ℃. When it comes to the optimization design of fluid machinery,

146   the genetic algorithm (GA), simulated annealing algorithm, particle swarm

147   optimization (PSO) and ant colony optimization (ACO) are frequently used. Since the

148   GA can deal with complex optimization problems and is less sensitive to the initial

149   conditions, it is distinguished from other optimization methods with respect to the

150   optimization design of turbines for ORC systems, and is the most widely used method

151   to select parameters about the turbine size [13], stage geometry [15, 40] and turbine

152   performance.

153   In the conventional design of the ORC system, the turbine efficiency is a fixed

154   value. But in practical application, the turbine efficiency is directly related with the

155   selected working fluids and the system operating conditions. At the same time, the

156   system parameter determination is also influenced by the turbine performance. It's

157   necessary to couple the modeling of ORC system with the preliminary design of

158   radial-inflow turbine. Song et al. [41] presented a 1-D analysis model of the

159   radial-inflow turbine in the ORC system design with seven key parameters

160   determining the turbine geometry and aerodynamic performance as fixed values. Pan

161   and Wang [42] replaced the constant isentropic efficiency with the internal efficiency

162   of optimal radial turbine for each condition and analyzed the effects of evaporating

163   temperature on cycle performance. This study focused on the optimization of degree

164   of reaction, hub-diameter ratio and peripheral velocity ratio while remaining other

165   parameters constant. Jubori et al. [43] presented an integrated approach combining

166   ORC system modeling, mean-line design and 3-D CFD analysis for micro-scale axial

167   and radial-inflow turbines with the maximum total-to-total efficiency as 83.48% and

168   83.85%, respectively. It appears from the previous investigations that the existing

169   research aforementioned mainly focused on the study of ORC system or radial turbine

only. To the best of the authors' knowledge, however, the exploration of the coupled design of the ORC system and its radial-inflow turbine has been far from complete and there is still much room to be enhanced in this area. Moreover, the recommended values of the key design parameters for the ORC radial-inflow turbine are not extensively studied.

In this paper, an ORC model is built for the utilization of geothermal resource with heat source inlet temperature of 120 ℃. A coupled design of the ORC system and the radial-inflow turbine is performed with the constrained GA to maximize the turbine efficiency. The ORC systems with different heat source outlet temperatures and working fluids are investigated by an original MATLAB code. The analysis of the optimized parameters: degree of reaction, velocity ratio, loading coefficient, flow coefficient, ratio of wheel diameter and rotational speed, is conducted. In addition, this paper also provides references on the recommended ranges of the key design parameters for ORC radial-inflow turbine based on the optimized results.

Nomenclature

Symbol

W	work/power, W
Q	heat, J
h	specific enthalpy, J/kg
Δh_{actual}	actual enthalpy drop, J/kg
Δh_s	isentropic enthalpy drop, J/kg
Δh	enthalpy difference, J/kg
T	temperature, K
P	pressure, Pa
ρ	density, kg/m^3
c	absolute velocity, m/s
w	relative velocity, m/s
u	peripheral velocity, m/s
m	mass flow rate, kg/m^3
r	radius, m
d	diameter, m
b	blade height, m
τ	blockage factor
h_c	tip clearance, m
E	energy, factor
H	form factor
C	loss coefficient multiplier, 1
l	surface length, m
s	blade spacing at blade-row exit, m
A	area, m^2
t	trailing-edge thickness, m
Z	blade number
Ma	Mach number
$d_{2,s}$	diameter at the rotor shroud, m
$d_{2,h}$	diameter at the rotor hub, m
$d_{2,sh}$	mean diameter at the rotor outlet, m

Subscripts

wf	working fluid
0	nozzle inlet
1	nozzle outlet or rotor inlet
2	rotor outlet
$cond$	condenser
$evap$	evaporator
s	isentropic process
n	nozzle
r	rotor
m	meridional direction
u	peripheral direction
2-D	two dimensional
3-D	three dimensional
rel	relative
abs	absolute

Greek letters

η_{1st}	the first law efficiency of ORC system
$\eta_{turbine}$	turbine efficiency
α	absolute flow angle, degree
β	relative flow angle, degree
Ω	degree of reaction
φ	nozzle velocity coefficient
ψ	rotor velocity coefficient
Φ	flow coefficient
Ψ	loading coefficient
μ	dynamic viscosity, Pa·s
ξ	loss coefficient
ζ	energy loss coefficient
θ	momentum thickness, m
γ	flow angle, degree
ω	rotational speed, rpm

195

196

197

198

2. ORC modeling and working fluid candidates

200   2.1 ORC modeling

201   Fig. 1 shows the schematic diagram of a basic ORC system, which includes four

202   main components: working fluid pump, evaporator, turbine and condenser. The

203   temperature-entropy diagram of the basic ORC using pentane is shown in Fig. 2.
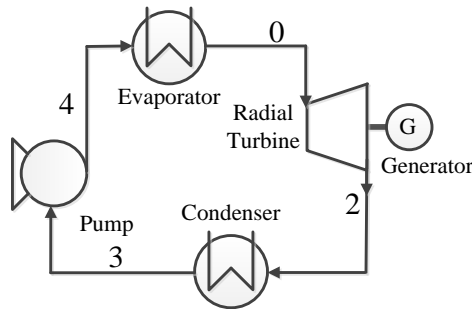

204
205   Fig.1. Schematic diagram of the basic ORC

206
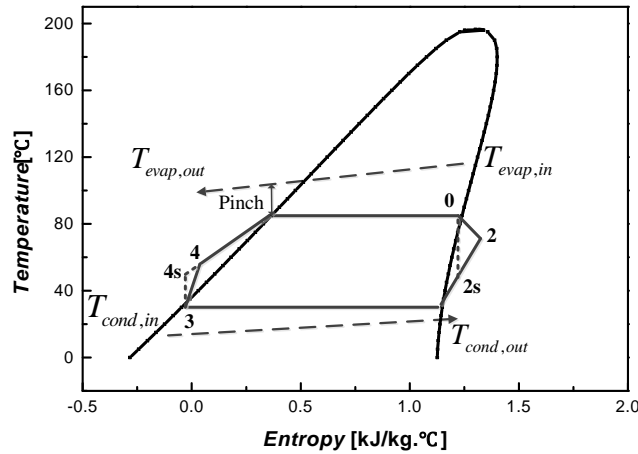207   Fig.2. Temperature-entropy curve of the basic ORC (using pentane)

208   The work consumed by the pump in the process 3 to 4 is expressed by:

209    $W_{pump} = m_{wf}(h_4 - h_3) = m_{wf}(h_{4s} - h_3)/\eta_{pump}$ (1)

210   The heat absorbed in the evaporator in the process 4 to 0 is expressed by:

211    $Q_{evap} = m_{wf}(h_0 - h_4) = m_{evap}(h_{evap,in} - h_{evap,out})$ (2)

212   The work produced by the turbine in the process 0 to 2 is expressed by:

213    $W_{turb} = m_{wf}(h_0 - h_2) = m_{wf}(h_0 - h_{2s}) \cdot \eta_{turbine}$ (3)

214 The heat generated in the condenser in the process 2 to 3 is expressed by:

215 $$Q_{cond} = m_{wf}(h_2 - h_3) = m_{cond}(h_{cond,out} - h_{cond,in})$$ (4)

216 The net power output of the ORC system is expressed by:

217 $$W_{net} = W_{turbine} - W_{pump}$$ (5)

218 The first law efficiency of the ORC system can be calculated by:

219 $$\eta_{1st} = \frac{W_{net}}{Q_{evap}} = \frac{W_{turbine} - W_{pump}}{Q_{evap}} = \frac{(h_0 - h_2) - (h_4 - h_3)}{h_0 - h_4}$$ (6)

220 The conditions for the heat source, heat sink and ORC system are summarized in

221 Table 1. The working conditions are applied to the utilization of geothermal resource

222 with fixed heat source temperature and mass flow rate.

223 Table 1 Working conditions for the heat source, heat sink and cycle parameters

System	Parameters	Value
Heat source (water)	Inlet temperature (ºC)	120
	Pressure (kPa)	500
	Mass flow rate (kg/s)	10
Heat sink (water)	Inlet temperature (ºC)	25
	Outlet temperature (ºC)	35
	Pressure (kPa)	250
ORC	Isentropic pump efficiency	0.8
	Pinch temperature in the evaporator (ºC)	12
	Pinch temperature in the condenser (ºC)	8

224 2.2 Working fluid candidates

225 Working fluid plays an important role in the design and performance analysis of

226 an ORC system. It not only affects the turbine aerodynamic performance but also its

227 geometry. Generally, the organic working fluids are divided into three categories: wet,

228 dry and isentropic in terms of the slope of the saturated vapor line in the T-s diagram.

229 Due to the low temperature of the heat source, this study selects four commonly used

230 dry working fluids, pentane, R245fa, R365mfc and R123 [13, 36, 44]. This ensures

231 that there are no liquid working fluids existing in the rotor and thus there is no need to

232 superheat the working fluids. Table 2 shows the properties of the selected working

233 fluid candidates.

234 Table 2 Properties of the working fluid candidates

Fluid	Molecular weight (g/mol)	Critical pressure (kPa)	Critical temperature (°C)	Normal boiling point (°C)	GWP (100 yr)	ODP
Pentane	72.15	3370	196.55	36.06	20	0
R245fa	134.05	3651	154.01	15.14	950	0
R365mfc	148.07	3266	186.85	40.15	794-997	0
R123	152.93	3662	183.68	27.82	77	0.02

3. Turbine design

236 The preliminary design of the radial turbine is performed by the mean-line

237 approach, which is on the basis of a one-dimensional assumption that there is a mean

238 streamline through the stage [13]. Conservation of mass, momentum and energy

239 together with velocity triangle equation, state equation and loss model are used to

240 determine the parameters of basic geometry, velocity triangles, thermodynamic

241 properties. In this paper, volute and expansion diffuser are ignored in order to simplify

242 computational load. The simplified working procedure is shown in Fig. 3, where point

243 0 represents the state of the working fluid at the nozzle inlet, point 1 represents the

244 state at the nozzle outlet as well as the state at the rotor inlet, and point 2 represents

245 the state at the rotor outlet. Δh_s is the isentropic enthalpy drop of the entire turbine

246 and Δh_{actual} is the actually useful enthalpy drop which does not account for the

247 energy of leaving velocity.
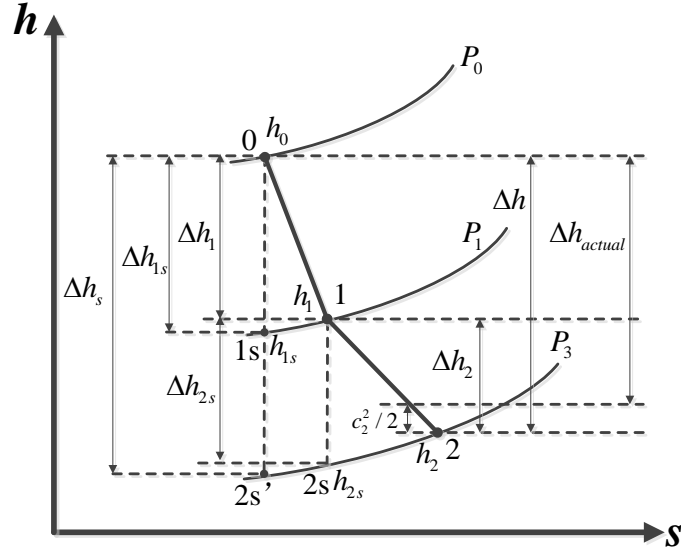
Fig.3. *h-s* diagram of the radial-flow turbine
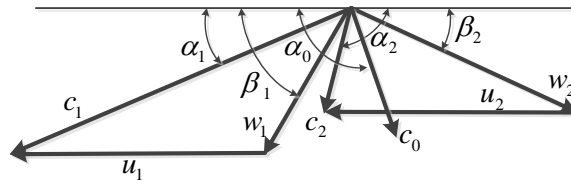
Absolute velocity, relative velocity and velocity angles at the nozzle outlet and

rotor outlet are determined according to velocity triangles of the radial-inflow turbine

as shown in Fig. 4.

Fig.4. Velocity triangles of the radial-inflow turbine

As shown in Fig. 3, working fluid flows through the nozzle and rotor. From state

point 0 to state point 1, the flow equations of the working fluid can be expressed as

follows, where the subscripts 0, 1 and 2 represent the same state point in Fig. 3:

Mass continuity equation: $m_{wf} = \rho_1 c_{1m} b_{1n} d_{1n} \pi \tau_n$ (7)

Energy equation: $\begin{cases} \Delta h_{1s} = (1-\Omega) \cdot \Delta h_s, h_{1s} = h_0 - \Delta h_{1s} \\ h_1 = h_{1s} + (c_{1s}^2 - c_1^2)/2 = h_{1s} + c_{1s}^2 (1-\varphi^2)/2, c_1 = \varphi c_{1s} \end{cases}$ (8)

Equation of state: $P_1 = f(h_{1s}, s_0), T_1 = f(P_1, h_1), \rho_1 = f(P_1, h_1)$ (9)

Velocity triangle: $u_1 = (u_1/c_s) \cdot c_s, c_{1m} = \Phi \cdot u_1, c_{1u} = \sqrt{c_1^2 - c_{1m}^2}$ (10)

262 where τ_n is the nozzle blockage factor. c_s $(=\sqrt{2\Delta h_s})$ is the ideal velocity of the

263 working fluid at the turbine outlet. c_{1m} and c_{1u} are the absolute velocity in the

264 meridional and peripheral directions at the nozzle outlet, respectively. φ is the nozzle

265 velocity coefficient. u_1 / c_s is the velocity ratio. Φ is the flow coefficient

266 ($\Phi = c_{1m} / u_1$). Ω is the degree of reaction. b_{1n} is the nozzle blade height and d_{1n} is

267 the nozzle outlet diameter.

268   From state point 1 to state point 2, the flow equations of the working fluid can be

269 expressed as follows:

270 Mass continuity equation: $m_{wf} = \rho_1 c_{1m} b_1 d_1 \pi \tau_1 = \rho_2 c_{2m} b_2 \pi \cdot (d_{2,s} + d_{2,h}) / 2 \cdot \tau_2$ (11)

271 Energy equation: $\begin{cases} h_2 = h_{2s} + (w_{2s}^2 - w_2^2)/2 + L_{df} + L_c \\ \quad = h_{2s} + w_{2s}^2 (1 - \psi^2)/2 + L_{df} + L_c, w_2 = \psi w_{2s} \end{cases}$ (12)

272 Equation of state: $T_2 = f(P_2, h_2), \rho_2 = f(T_2, h_2)$ (13)

273 Velocity triangle: $u_2 = \mu u_1, c_{2u} = (c_1 \cdot \cos\alpha_1 \cdot u_1 - u_1^2 \cdot \Psi) / u_2, c_{2m} = \sqrt{c_2^2 - c_{2u}^2}$ (14)

274 where τ_1 and τ_2 are the rotor inlet and outlet blockage factors, respectively. c_{2m}

275 and c_{2u} are the absolute velocity in the meridional and peripheral directions at the

276 rotor outlet, respectively. ψ is the rotor velocity coefficient. μ is the ratio of wheel

277 diameter ($\mu = d_{2,sh} / d_1$). Ψ is the load coefficient ($\Psi = (u_1 c_{1u} - u_2 c_{2u}) / u_1^2$). b_1 is the

278 nozzle blade height and d_1 is the nozzle outlet diameter. $d_{2,s}$ and $d_{2,h}$ are the

279 diameter at the rotor shroud and hub, respectively. L_{df} and L_c are the disk-friction

280 loss and tip clearance loss, respectively.

281   Five kinds of turbine loss are taken into consideration in the preliminary design,

282 including the nozzle passage loss, rotor passage loss, leaving velocity loss,

283 disk-friction loss and tip clearance loss. The nozzle passage loss coefficient (ξ_n), rotor

284 passage loss coefficient (ξ_r) and leaving velocity loss coefficient (ξ_e) are expressed

285 as follows:

286 $$\xi_n = \left(1 - \varphi^2\right)\left(1 - \Omega\right) \tag{15}$$

287 $$\xi_r = \left(w_2 / c_s\right)^2 \left(1/\psi^2 - 1\right) \tag{16}$$

288 $$\xi_e = \left(c_2 / c_s\right)^2 \tag{17}$$

289 Disk-friction loss (L_{df}) and coefficient (ξ_{df}), tip clearance loss (ξ_c) and coefficient

290 (L_c) are expressed as follows [45]:

291 $$\xi_{df} = \frac{0.02125 \rho_1 u_1^3 r_1^2}{\left(\frac{\rho u r}{\mu}\right)_1^{0.2} \cdot m_{wf} \cdot \Delta h_s} \tag{18}$$

292 $$L_{df} = \xi_{df} \cdot \Delta h_s \tag{19}$$

293 $$\xi_c = \frac{h_c}{r_{2,s} - r_{2,h}} \tag{20}$$

294 $$L_c = \xi_c \cdot \Delta h_s \tag{21}$$

295 where h_c is the tip clearance, specified as 0.3mm. This loss model assumes that the

296 fractional loss due to tip clearance equals to the ratio of clearance to passage height at

297 the rotor exit.

298 Turbine efficiency (total to static efficiency) is expressed as:

299 $$\eta_{turbine} = \frac{\Delta h_{actual}}{\Delta h_s} = \frac{\Delta h - c_2^2 / 2}{\Delta h_s} \tag{22}$$

300   The power output is calculated as follows:

301    $W = \Delta h_{actual} m_{wf} \eta_{turbine}$ (23)

302   **4. Coupled model of ORC and radial-inflow turbine with genetic algorithm**

303   4.1 Velocity coefficient

304   According to Eqs. (7)-(14), nozzle velocity coefficient (φ), rotor velocity

305   coefficient (ψ), degree of reaction (Ω), velocity ratio (u_1/c_s), loading coefficient

306   (Ψ), flow coefficient (Φ), ratio of wheel diameter (μ) are seven key dimensionless

307   parameters when designing the radial-inflow turbine. In the preliminary design of

308   conventional turbine, φ and ψ are estimated and specified according to the

309   empirical formula since they are dependent on many factors, such as the blade profile,

310   machining precision, fluid flow conditions and so forth. This study uses the loss

311   models proposed by the Lewis Research Center [45] to calculate these two parameters

312   iteratively. The relationships of φ and ψ with nozzle and rotor energy loss

313   coefficients (ζ_n and ζ_r) are as follows:

314    $\varphi = \sqrt{1-\zeta_n}$, $\psi = \sqrt{1-\zeta_r}$ (24)

315   ζ_n and ζ_r can be expressed in a unified formula:

316    $$\zeta_{3D} = \frac{EC\left(\frac{\theta_{tot}}{l}\right)_{ref}\left(\frac{Re}{Re_{ref}}\right)^{-0.2}\left(\frac{l}{s}\right)\left(\frac{A_{3D}}{A_{2D}}\right)}{\cos\gamma - \frac{t}{s} - HC\left(\frac{\theta_{tot}}{l}\right)_{ref}\left(\frac{Re}{Re_{ref}}\right)^{-0.2}\left(\frac{l}{s}\right)}$$ (25)

317   where E is the energy factor and H is the form factor, which presents the

318   characteristics of boundary layer flow and can be calculated by empirical equations. C

319   is the loss coefficient multiplier. Re is the Reynolds number. θ is the momentum

320   thickness. l is the surface length from leading edge to trailing edge. s is blade spacing

321   at blade-row exit. A_{3D} / A_{2D} represents the 3-D to 2-D area ratio. γ is the flow

322   angle from the throughflow direction. t is the trailing-edge thickness. All these related

323   factors are discussed in detail in [45] and can be calculated according to the

324   corresponding formulas. Some parameters need to be known in advance in order to

325   complete the preliminary design of the radial-inflow turbine and obtain some

326   parameters related to the geometry: the tip clearance value is fixed as 0.3mm

327   considering the manufacture technology; the radial clearance between nozzle and

328   rotor is specified as 1 mm [46]; the nozzle solidity is specified as 1.3 according to [47].

329   Nozzle blade uses the TC-4P blade profile which is a commonly used stator profile in

330   the ORC system and thus the nozzle inlet absolute flow angle α_0 can be obtained.

331   Initial φ and ψ are presupposed in advance to finish the preliminary design of the

332   radial-inflow turbine. Then ζ_n and ζ_r can be calculated by Eq. (25), after which φ

333   and ψ are updated by Eq. (24) to proceed to the next iteration until the differences in

334   velocity coefficients of two iteration are within a minimum range.

335   4.2 Optimization method

336   In addition to the other five dimensionless parameters (Ω, u_1 / c_s, Ψ, Φ, μ),

337   rotational speed (ω) should also be optimized since its optimal value varies with

338   operating conditions. In this work, turbine efficiency is specified as the objective

339   function to optimize the radial-inflow turbine for each operating condition since under

340   this condition the optimized results of the power output as the optimization objective

341   are very similar to that of the turbine efficiency as the optimization objective.

342   The six optimized variables are limited by empirical values, as listed in Table 3.

343

Table 3 Recommended value ranges of the six optimized variables

Design variables	Range	Reference
Degree of reaction (Ω)	0.50-0.60	[48]
Velocity ratio (u_1/c_s)	0.69-0.71	[36]
Loading coefficient (Ψ)	0.85-1.00	[38]
Flow coefficient (Φ)	0.15-0.30	[38]
Ratio of wheel diameter (μ)	0.50-0.60	[46]
Rotational speed (ω, rpm)	12000-25000	[38]

345   Some optimization constraints are implemented in this model to ensure the

346   reasonable results of optimized turbine in terms of high aerodynamic performance and

347   ease of manufacture.

348   • The nozzle outlet absolute blade angle α_1 is recommended between 12-30°

349   and the rotor outlet relative blade angle β_2 is recommended between 20-45° [46].

350   These values are established with the trade-off between the high stage shaft power and

351   low flow losses.

352   • The ratio of the rotor inlet blade height and diameter is considered to lie

353   between 0.03 and 0.1 [46]. This value is set to limit the rotor tip clearance losses.

354   • The nozzle outlet Mach number is limited less than 1.5 to lower the supersonic

355   loss at the rotor inlet.

356   • The hub ratio (rotor exit hub to inlet radius ratio, $d_{2,h}/d_1$) is set more than 0.2

357   since the smaller hub ratio leads to great difficulty in assigning blades at the hub [44].

358   In this work, the genetic algorithm (GA) is used to complete the optimization of

359   the six key design parameters. The GA is a global optimum algorithm based on the

360   theory of biological evolution [49]. Compared with other optimization methods, the

361   GA has many advantages. It can not only deal with complex optimization problems

362   such as non-linear and multi-dimensional but also is less sensitive to the initial

363   conditions. Therefore, the GA is widely used in many literatures about ORC systems

364   [13, 15, 40]. In the basic GA, the initial population of individuals is generated

365   randomly from the prescribed range of optimization variables. All individuals in every

366   generation are assessed in terms of their fitness values. A new generation of

367   individuals is generated by selecting the current population according to their fitness

368   values, crossovering the selected members according to the crossover rate and

369   mutating certain individuals according to the mutation rate. Therefore, selection,

370   crossover and mutation are the three main operations in GA. The flowchart of the

371   constrained GA is shown in Fig. 5. The control operators of GA are listed in Table 4.
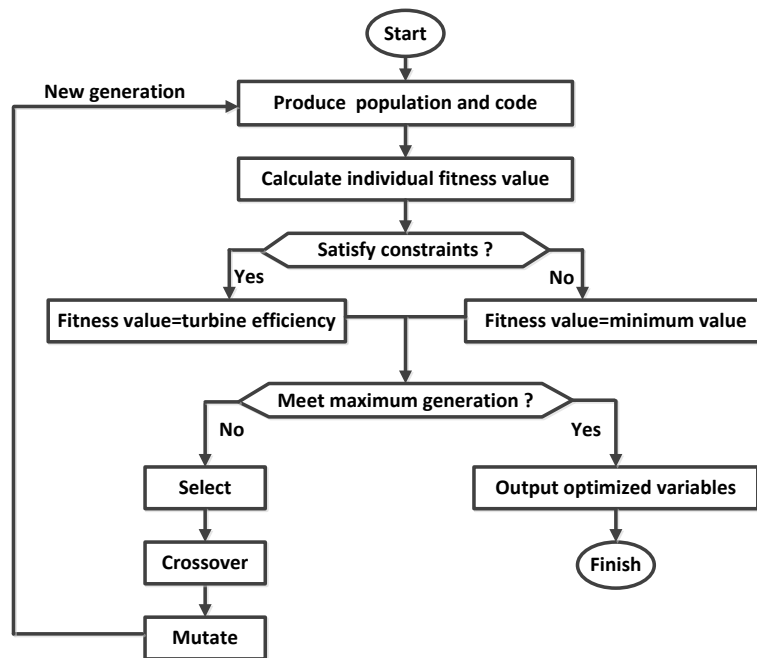
372

373   Fig.5. Flowchart of the constrained GA

374   Table 4 Control operators of GA

Operator	Value
Maximum number of generations	200
Number of individuals	80
Selection rate	0.9
Crossover probability	0.7
Mutation rate	0.01

375   4.3 Simulation method

376   Fig. 6 shows the flowchart of the simulation process of the ORC system, in

377   which the optimization design of the radial-inflow turbine with constrained GA is

378   introduced. The pinch methodology is used here to simulate the ORC cycle. To

379   simplify the ORC modeling, the turbine inlet and condenser outlet are assumed to be

380   saturated vapor state and saturated liquid state, respectively. The turbine efficiency is

381   varying with the operation conditions of the ORC system instead of being constant in

382   the conventional ORC system design. Three initial input parameters, turbine inlet

383   temperature (T_0), condenser outlet temperature (T_3), and turbine efficiency ($\eta_{turbine}$)

384   are estimated as the initial input data to start the simulation. In the preliminary

385   optimization design, constrained GA optimizes six key parameters in the experience

386   value range as listed in Table 4, and the iterative solving process determines the

387   velocity coefficients of nozzle and rotor. After each loop, the newly obtained values of

388   the turbine inlet and outlet temperature as well as the condenser outlet temperature are

389   updated. If the requirements of the three parameters are not reached as shown in Fig. 6,

390   they are used again as the initial input data to continue the next loop. However,

391   initially turbine efficiency is estimated instead of the turbine outlet temperature. This

392   is because at the beginning it is difficult to estimate the turbine outlet temperature

393   while turbine efficiency can be estimated by experience. The process is repeated until

394   the requirements of the turbine outlet temperature, the pinch temperature in the

395   evaporation and condenser are met. Pinch point in the evaporation appears at the

396   saturated liquid state of the working fluids and pinch point in the condenser appears at

397   the saturated vapor state of the working fluids. An original MATLAB code is

398   programmed to simulate the described ORC system and optimization design of

399   radial-inflow turbine. The properties of working fluids are obtained from REFPROP

400   9.0 [50]. The simulation is assumed to operate at the steady state and to neglect the

401   pressure and heat losses in the entire cycle.
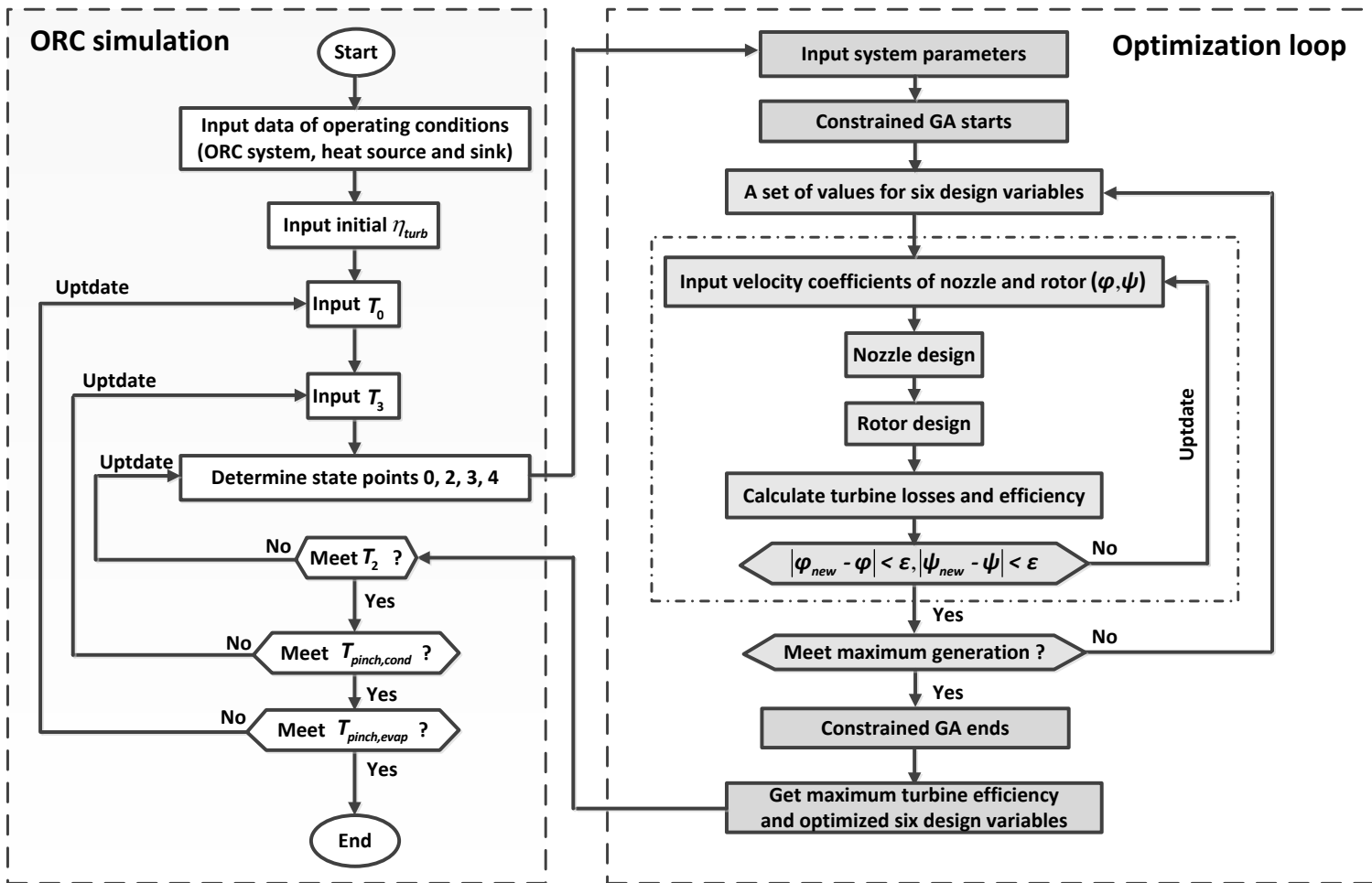
402   Fig.6. Flowchart of the coupled ORC-turbine model

403   **5. Results and discussion**

404   5.1 Validation of the turbine design model

405   The turbine design model described in section 3 is validated by the comparison

406   of the developed codes with other published codes: Glassman [45], commercial radial

407   turbine design software RITAL from Concepts NREC [51] and Rahbar et al. [52]. The

408   testing conditions are from Glassman case [45] and the results of different codes are

409   shown in Table 5. The set of results from the developed model in this work shows a

410 good agreement with both the original one and literature in terms of flow

411 characteristic, turbine principal geometry and overall performance. It should be

412 noticed that the turbine total-to-static efficiency predicted by the developed code in

413 this work is closer to the original efficiency than the other two kinds of codes.

414 Therefore, the turbine design model is considered to be validated for the coupled

415 modeling of ORC system and its radial-inflow turbine.

416 <center>Table 5 Comparison of developed code with published codes</center>

Paramter	Glassman [45]	RITAL [51]	Rahbar et al. [52]	Present code
Stator				
Inlet radius, m	0.09775	0.1033	0.09911	—
Outlet radius, m	0.07983	0.08268	0.08133	0.07795
Outlet absolute flow angle, deg.	18	26.61	21.89	18.09
Rotor				
Inlet radius, m	0.0777	0.07874	0.07888	0.07695
Outlet hub radius, m	0.01936	0.02362	0.02312	0.01995
Outlet shroud radius, m	0.05542	0.05591	0.05546	0.0546
Inlet absolute flow angle, deg.	18.08	26.87	26.49	18.09
Inlet relative flow angle, deg.	121.5	116.27	116.64	123.55
Outlet absolute flow angle, deg.	90	90.01	90	90.56
Outlet relative flow angle, deg.	35.10	34.42	36.24	35.1399
Total-to-static efficiency, %	82	79	78.8	79.45
Power, kW	22.371	—	—	21.52

417 5.2 Optimization results

418 The turbine design model validated in section 5.1 is used to study the coupled

419 modeling of ORC system and its radial-inflow turbine, and to investigate the influence

420 of heat source temperature. The overall examined range of the heat source outlet

421 temperature is set from 110 ℃ to 80 ℃. For pentane and R245fa the temperature

422 range is 80-105 ℃ while for R365mfc and R123 the temperature range is 90-110 ℃.

423 Out of these ranges, certain design parameters of the radial-inflow turbine cannot

424 satisfy the constraints proposed in section 4 and thus there is no data at this point. The

425 variations of pressure ratio and mass flow rate with the outlet temperature of the heat

426 source are first shown in Fig. 7.
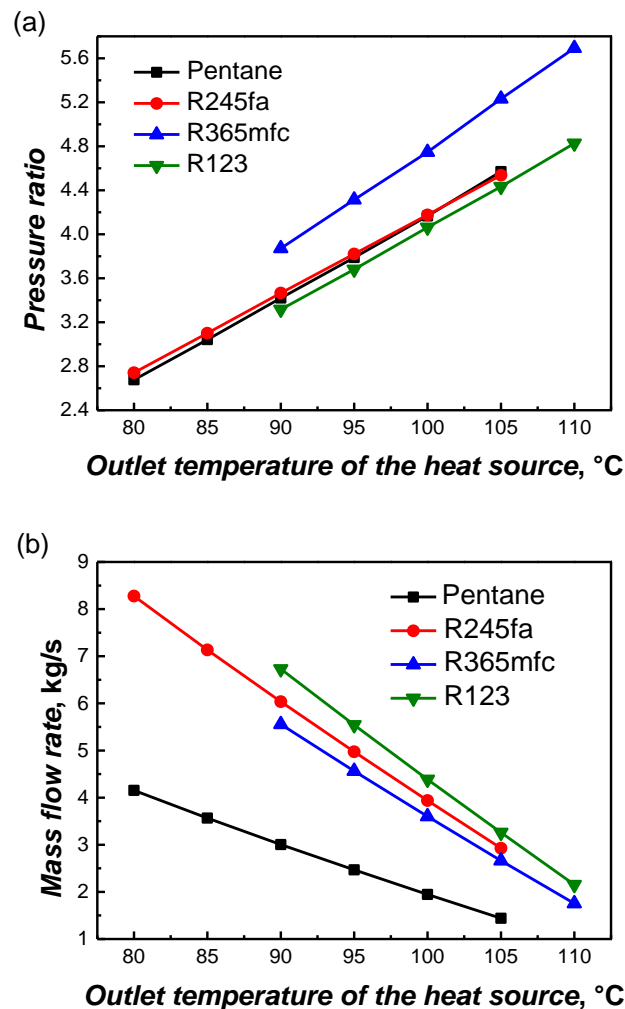
427

428

429 Fig.7. Variations of (a) pressure ratio and (b) mass flow rate with the outlet temperature of the heat
430   source

431   Under the condition of fixed mass flow rate for the heat source, as the outlet

432 temperature of the heat source decreases, more heat load is absorbed by the ORC

433 system and thus the mass flow rate of the working fluids increases. The cycle using

434 R123 has the highest mass flow rate at any conditions while using pentane has the

435 lowest mass flow rate. The lower outlet temperature of the heat source causes the

436 evaporation temperature to decrease and thus to lower the pressure ratio. R365mfc has

437   the highest pressure ratio at each condition while for pentane, R245fa and R123 the

438   pressure ratios are similar.
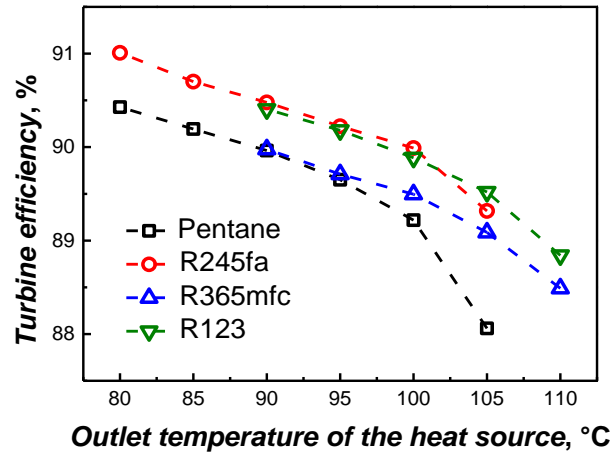

439

440   Fig.8. Variation of turbine efficiency with the outlet temperature of the heat source

441   The turbine efficiency depending on different working fluids and heat source

442   temperature conditions are shown in Fig. 8. The optimized turbine efficiency varies

443   from 88.06% using pentane at the heat source outlet temperature of 105 ºC to 91.01%

444   using R245fa at the heat source outlet temperature of 80 ºC. Fig. 8 also shows that the

445   turbine efficiency decreases with the increase of the heat source outlet temperature.

446   This indicates that smaller pressure ratio and larger mass flow rate enhance the turbine

447   efficiency. In addition, the decreasing rate of turbine efficiency becomes faster when

448   the heat source outlet temperature is greater than 100 ºC, especially for pentane and

449   R245fa. R123 and R365mfc also have this similar trend but the decreasing rate is

450   respectively less intense. This can be explained by the loss distribution shown in Fig.

451   9, which illustrates the variations of five kinds of losses related with the heat source

452   outlet temperature using pentane and R123 as working fluids. Fig. 9 shows that the

453   rotor passage loss has the highest contribution for all the examined working fluids. As

454   the outlet temperature of the heat source increases, the rotor passage loss increases

455   gradually, especially violently when the heat source outlet temperature is greater than

456 100 ℃. For pentane and R245fa, when the heat source outlet temperature increases

457 from 100 ℃ to 105 ℃, the increasing rate of the rotor passage loss coefficient is 20.92%

458 and 17.05%, respectively. While for R365mfc and R123 the change rate is within

459 4.5%. This great increase of the rotor passage loss accounts for the sudden drop of the

460 turbine efficiency using pentane and R245fa. Since the pressure ratio increases with

461 the higher outlet temperature of the heat source, the velocity at rotor becomes larger

462 leading to higher rotor passage loss. In addition, the loss distribution is similar for all

463 the examined working fluids with the rotor passage loss having the highest

464 contribution, varying from 32.15% to 37.40% of the total losses. The nozzle passage

465 loss, rotor passage loss and leaving velocity loss are diverse in the same order of

466 magnitude. Disk-friction loss and tip clearance loss are one magnitude lower than the

467 above three kinds of losses. As shown in Fig. 9, both the disk-friction loss and tip

468 clearance loss increase with the rise of the heat source outlet temperature. This is

469 consistent with the conclusion that high expansion ratio leads to high friction loss

470 [42].
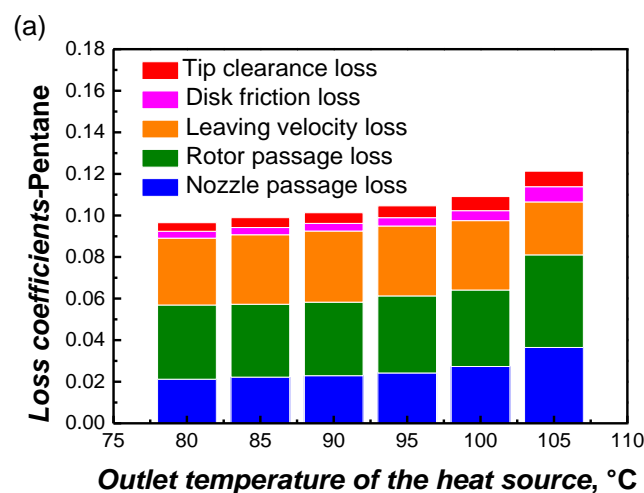
471
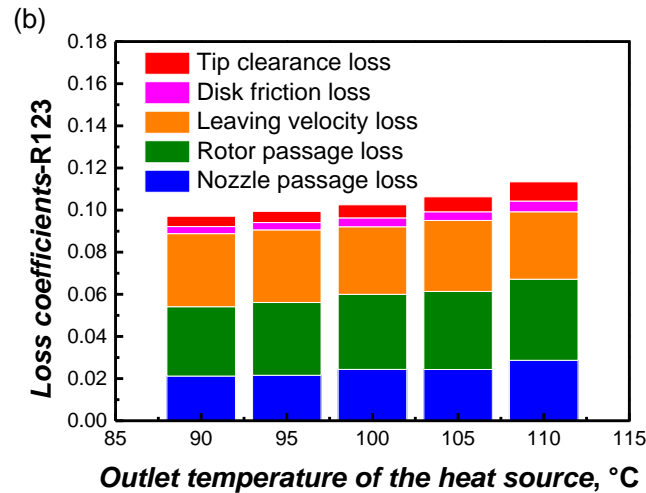
(b)

Fig.9. Variations of the five kinds of losses with the outlet temperature of the heat source using pentane and R123

The simulated results of the cycle efficiency, net power output and specific net power per mass flow rate are successively plotted in Fig. 10, Fig. 11 and Fig. 12. Fig. 10 shows the cycle efficiency increases with the rise of the heat source outlet temperature while the net power has the opposite trend. This is due to the fact that the mass flow rate of the working fluids increases and enthalpy drop decreases with the lower heat source outlet temperature, but the increase degree of the mass flow rate is much larger than the decrease degree of the enthalpy drop, which accounts for the increase of the net power. Take R123 for example, the enthalpy drop is -23.23% while the increase of the mass flow rate is 212.60% when the outlet temperature of the heat source changes from 110 ℃ to 90 ℃. Moreover, it can be noticed that the differences of both the cycle efficiency and the net power output among different working fluids at each condition are not substantial. As shown in Fig. 12, the specific net power per mass flow rate increases with the higher heat source outlet temperature. Though the turbine efficiency using pentane is the lowest at each condition presented in Fig. 8, the specific net power is much higher than the other three kinds of working fluids. This indicates that pentane has the highest enthalpy drop among the examined working

491   fluids. In the situation where the inlet temperature of the heat source rather than the

492   absorbed heat load is fixed, the ORC cycle efficiency and the net power output change

493   monotonously with the heat source outlet temperature, but their variation trends are in

494   the opposite direction. From the perspective that the net power output is the main aim

495   of the ORC system, the lower the outlet temperature of the heat source is, the better.

496   Among the four examined working fluids, R123 achieves the maximum cycle

497   efficiency of 12.21% together with the turbine efficiency of 88.84% at the heat source

498   outlet temperature of 110 ºC. R245fa achieves both the maximum net power output of

499   138.74 kW and the maximum turbine efficiency of 91.01% at the heat source outlet

500   temperature of 80 ºC.
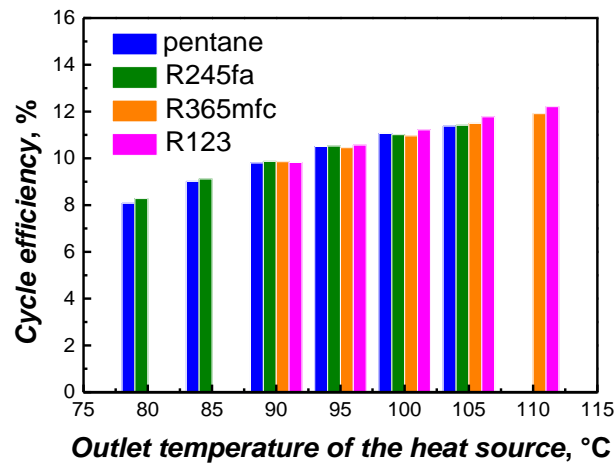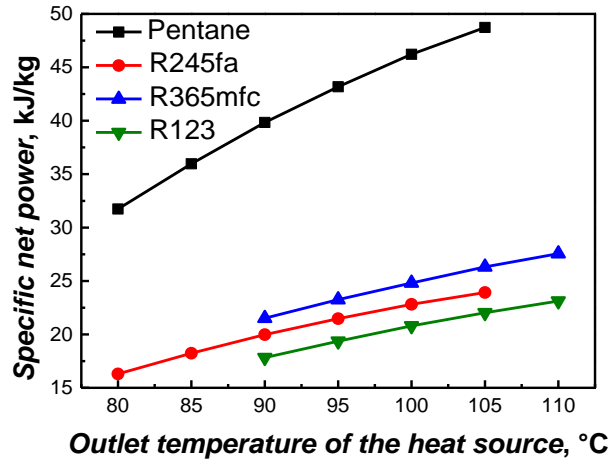

501

502   Fig.10. Variation of cycle efficiency with the outlet temperature of the heat source
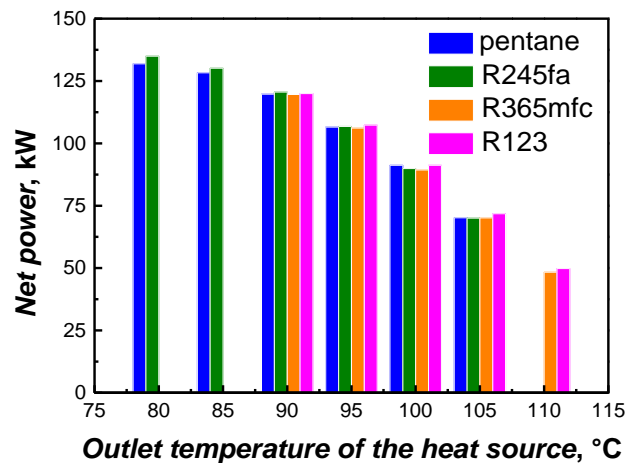
503

504 Fig.11. Variation of net power with the outlet temperature of the heat source

505

506 Fig.12. Variation of specific net power with the outlet temperature of the heat source
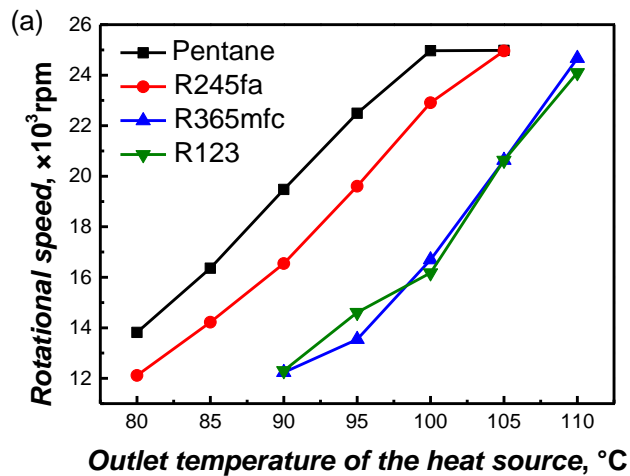
507 In the following section a thorough analysis of the optimized results of the six

508 key design parameters is conducted to provide references for ORC radial-inflow

509 turbine in the low temperature range. Fig. 13 shows the optimized results of rotational

510 speed, overall diameter (d_0) and Mach number at the rotor inlet with the outlet
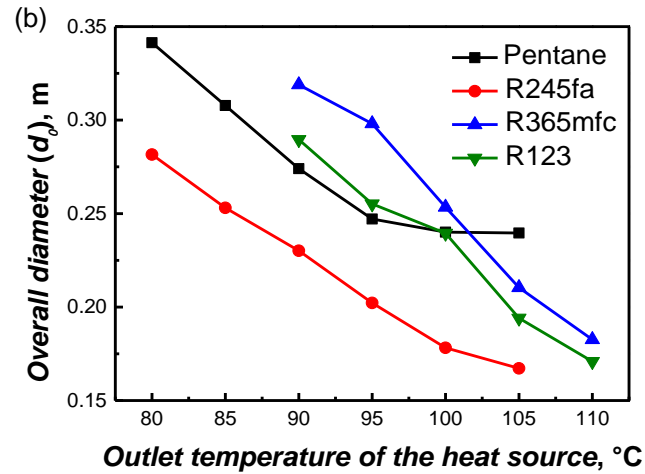
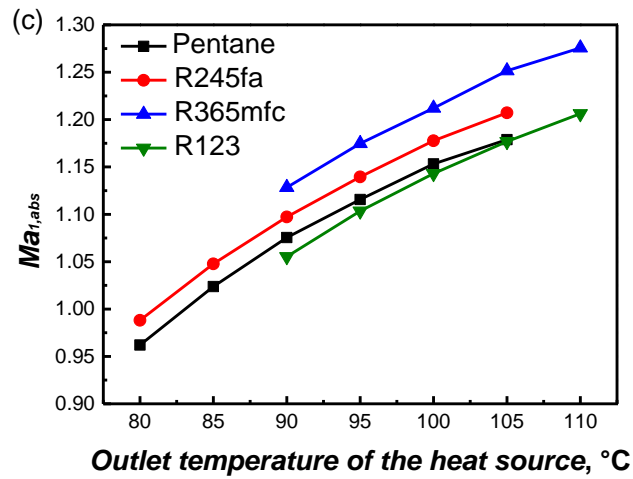511 temperature of the heat source.

512

(b)

(c)

Fig.13. Variation of rotational speed (a), overall diameter (b) and Mach number at the rotor inlet (c) with the outlet temperature of the heat source

As shown in Fig. 13, the rotational speed increases with the rise of the heat source outlet temperature. Since the enthalpy drop increases with the higher heat source outlet temperature, higher rotational speed is required to provide the larger peripheral speed and more wheel periphery work. Taking R245fa for example, the rotational speed increases from 12114 rpm to 24959 rpm when the heat source outlet temperature changes from 80 ℃ to 90 ℃, which amounts to 106.03% growth rate. In addition, pentane has the highest rotational speed at each condition. This is expected because pentane has the largest enthalpy drop among the examined fluids discussed previously. Fig. 13 also indicates that pentane reaches its rotational speed constraint

526   when the heat source outlet temperature is more than 100 ℃.

527   Considering the practicability of manufacture, some parameters related to the

528   turbine geometry, including the hub ratio ($d_{2,h}/d_1$), the inlet diameter of the turbine

529   (d_0) and the ratio of the rotor inlet blade height and diameter (b_1/d_1), restrict the

530   upper and lower limits of the heat source outlet temperature. For the examined

531   working fluids, as the outlet temperature of the heat source increases, the inlet

532   diameter of the turbine decreases because of the reduction in the mass flow rate of the

533   working fluids. The minimum overall diameter d_0 is achieved by R245fa at the heat

534   source outlet temperature of 105 ℃ (d_0=167.2mm) while the largest size is achieved

535   by pentane at the heat source outlet temperature of 80 ℃ (d_0=341.4mm). The rotor

536   exit hub to inlet radius ratio is in the range of 0.2017-0.2785 and is consistent with the

537   literature [15, 44]. Fig. 13 shows the variation of Mach number at the rotor inlet

538   ($Ma_{1,abs}$) with the outlet temperature of the heat source. $Ma_{1,abs}$ increases with the

539   higher heat source outlet temperature and R365mfc has the highest $Ma_{1,abs}$ at all

540   conditions because of combined effect of the high peripheral speed and low density

541   while R123 has the lowest. Except the condition of heat source outlet temperature of

542   80 ℃, all the examined working fluids have supersonic expansion at the rotor inlet,

543   which is undesirable. It indicates that it is appropriate to use the TC-4P blade profile

544   for nozzle since such kind of blade profile has lower loss in the transonic situation.

545   Based on the optimized results, the recommended ranges for the key six design

546   parameters can be made: the degree of reaction is recommended as 0.5-0.51; the

547   velocity ratio is recommended as 0.70-0.71; the loading coefficient is recommended

548   as 0.88-0.93; the flow coefficient is recommended as 0.26-0.29; the ratio of wheel

549   diameter is recommended as 0.51-0.6. Detailed results at the maximum turbine

efficiency condition are shown in Table 6.

Table 6 Optimized results of the preliminary design for the examined working fluids at the

maximum turbine efficiency condition

Parameters	Pentane, 80 ℃	R245fa, 80 ℃	R365mfc, 90 ℃	R123, 90 ℃
d_0 (m)	0.3414	0.2816	0.3189	0.2896
$b_{1,n}$ (m)	0.0175	0.0135	0.0145	0.0138
$d_{1,n}$ (m)	0.2625	0.2166	0.2452	0.2227
d_1 (m)	0.2605	0.2146	0.2432	0.2207
b_1 (m)	0.0180	0.0139	0.0149	0.0142
b_1 / d_1	0.0690	0.0646	0.0614	0.0643
$d_{2,s}$ (m)	0.2106	0.1730	0.1962	0.1782
$d_{2,h}$ (m)	0.0637	0.0498	0.0523	0.0553
Z_r	12	12	12	12
$Ma_{1,rel}$	0.2780	0.2868	0.3267	0.3065
$Ma_{1,abs}$	0.9621	0.9882	1.1284	1.0553
$Ma_{2,rel}$	0.5947	0.5987	0.6973	0.6618
$Ma_{2,abs}$	0.2481	0.2402	0.3054	1.0553
α_0 (deg.)	79.21	79.16	79.26	79.21
α_1 (deg.)	16.38	16.43	16.33	16.37
α_2 (deg.)	99.63	99.67	99.28	99.20
β_1 (deg.)	102.58	102.90	103.84	103.90
β_2 (deg.)	24.29	23.29	25.61	25.02
$\beta_{2,s}$ (deg.)	18.10	17.26	18.96	18.72
$\beta_{2,h}$ (deg.)	51.09	51.16	56.72	51.21
$d_{2,h} / d_1$	0.2445	0.2322	0.2151	0.2505
$\eta_{turbine}$ (%)	90.428	91.008	89.977	90.404

6. Conclusions

This paper proposes a coupled modeling of the ORC system and the radial-inflow turbine, which is designed by the mean-line approach with constrained GA to maximize the turbine efficiency. This model allows for the dynamic design of the ORC system and its radial-inflow turbine based on a wide range of operating conditions and a reasonable range of aerodynamic and geometric parameters. The

influences of heat source outlet temperature on the performance of ORC and radial-inflow turbine are investigated for pentane, R245fa, R365mfc and R123. It is found that the turbine efficiency decreases as the outlet temperature of the heat source increases with the minimum efficiency of 88.06% and maximum efficiency of 91.01%. Moreover, the cycle efficiency increases monotonously with the increase of the heat source outlet temperature while the net power output has the opposite trend. The maximum turbine and cycle efficiencies of 91.01%, 12.18% are obtained by R245fa at the heat source outlet temperature of 80 ºC and R123 at the heat source outlet temperature of 110 ºC, respectively. In addition, the recommended ranges for the degree of reaction, velocity ratio, loading coefficient, flow coefficient and ratio of wheel diameter of radial-inflow turbine are 0.5-0.51, 0.70-0.71, 0.88-0.93, 0.26-0.29 and 0.51-0.6, respectively. The minimum overall diameter d_0 (=167.2mm) is achieved by using R245fa at the heat source outlet temperature of 105 ºC.

Compared with other coupled design for ORC and radial-inflow turbine, this study introduces the constrained GA into the preliminary design of radial-inflow turbine with the prediction models of the velocity coefficients of nozzle and rotor. This coupled model is dynamic with the aim of achieving the maximum turbine efficiency. This study highlights the potential and effectiveness of this coupled modeling in design analysis for the ORC system and its radial-inflow turbine. Further work will concentrate on the CFD simulation or experimental testing of an ORC radial-inflow turbine.

References

[1] B. F. Tchanche, G. Papadakis, G. Lambrinos, A. Frangoudakis, Fluid selection for a low-temperature solar organic Rankine cycle, Applied Thermal Engineering, 2009,

584   29(11–12):2468–2476.

585   [2] A. M. Delgadotorres, L. Garcíarodríguez, Analysis and optimization of the

586   low-temperature solar organic Rankine cycle (ORC), Energy Conversion and

587   Management, 2010, 51(12):2846-2856.

588   [3] O. J. Besong, R. Taccani, M. D. Lucia, D. Micheli, G. Toniato, Development and

589   Experimental Characterization of a Small Scale Solar Powered Organic Rankine Cycle

590   (ORC), Associazione Termotecnica Italiana, 2016.

591   [4] A. M. Pantaleo, P. Ciliberti, S. Camporeale, N. Shah, Thermo-economic

592   Assessment of Small Scale Biomass CHP: Steam Turbines vs ORC in Different

593   Energy Demand Segments, International Conference on Applied Energy.

594   2015:1609-1617.

595   [5] S. K. Sansaniwal, M. A. Rosen, S. K. Tyagi, Global challenges in the sustainable

596   development of biomass gasification: An overview, Renewable and Sustainable

597   Energy Reviews, 2017, 80:23-43.

598   [6] S. Glover, R. Douglas, M. D. Rosa, X. Zhang, L. Glover, Simulation of a multiple

599   heat source supercritical ORC (Organic Rankine Cycle) for vehicle waste heat

600   recovery, Energy, 2015, 93:1568-1580.

601   [7] H. D. M. Hettiarachchi, M. Golubovic, W. M. Worek, Y. Ikegami, Optimum design

602   criteria for an Organic Rankine cycle using low-temperature geothermal heat sources,

603   Energy, 2007, 32(9):1698-1706.

604   [8] G. Cammarata, L. Cammarata, G. Petrone, Thermodynamic Analysis of ORC for

605   Energy Production from Geothermal Resources, Energy Procedia, 2014,

606   45:1337-1343.

607   [9] Q. Liu, A. Shen, Y. Duan, Parametric optimization and performance analyses of

608   geothermal organic Rankine cycles using R600a/R601a mixtures as working fluids,

609   Applied Energy, 2015, 148:410-420.

610   [10] A. Nemati, H. Nam, F. Ranjbar F, M. Yari, A comparative thermodynamic

611   analysis of ORC and Kalina cycles for waste heat recovery: A case study for CGAM

612   cogeneration system, Case Studies in Thermal Engineering, 2016, 9:1-13.

613   [11] G. Yu, G. Shu, H. Tian, Y. Huo, W. Zhu, Experimental investigations on a

614   cascaded steam-/organic-Rankine-cycle (RC/ORC) system for waste heat recovery

615   (WHR) from diesel engine, Energy Conversion and Management, 2016, 129:43-51.

616   [12] Y. M. Kim, G. S. Dong, G. K. Chang, G. B. Cho, Single-loop organic Rankine

617   cycles for engine waste heat recovery using both low- and high-temperature heat

618   sources, Energy, 2016, 96:482-494.

619   [13] K. Rahbar, S. Mahmoud, R. Aldadah, N. Moazami, Preliminary Mean-line Design

620   and Optimization of a Radial Turbo-Expander for Waste Heat Recovery Using Organic

621   Rankine Cycle, Energy Procedia, 2015, 75(3):860-866.

622   [14] K. K. Srinivasan, P. J. Mago, G. J. Zdaniuk, L. M. Chamra, K. C. Midkiff,

623   Improving the Efficiency of the Advanced Injection Low Pilot Ignited Natural Gas

624   Engine Using Organic Rankine Cycles, Journal of Energy Resources Technology,

625   2007, 130(2):333-342.

626   [15] M. Erbas, A. Biyikoglu, Design and multi-objective optimization of organic

627   Rankine   turbine,   International   Journal   of   Hydrogen   Energy,   2015,

628   40(44):15343-15351.

629   [16] E. H. Wang, H. G. Zhang, B. Y. Fan, M. G. Ouyangb, Y. Zhaoc, Q. H. Muc, Study

630   of working fluid selection of organic Rankine cycle (ORC) for engine waste heat

631   recovery, Energy, 2011, 36(5):3406-3418.

632   [17] R. Rayegan, Y. X. Tao, A procedure to select working fluids for Solar Organic

633   Rankine Cycles (ORCs), Renewable Energy, 2011, 36(2):659-670.

634   [18] U. Drescher, D. Brüggemann, Fluid selection for the Organic Rankine Cycle

635   (ORC) in biomass power and heat plants, Applied Thermal Engineering, 2007,

636   27(1):223-228.

637   [19] G. Qiu, Selection of working fluids for micro-CHP systems with ORC,

638   Renewable Energy, 2012, 48(6):565-570.

639   [20] J. Bao, L. Zhao, A review of working fluid and expander selections for organic

640   Rankine cycle, Renewable and Sustainable Energy Reviews, 2013, 24(10):325-342.

641   [21] B. Peris, J. Navarro-Esbrí, F. Molés, R. Collado, A. Mota-Babiloni, Performance

642   evaluation of an Organic Rankine Cycle (ORC) for power applications from low grade

643   heat sources, Applied Thermal Engineering, 2014, 75:763-769.

644   [22] K. Braimakis, S. Karellas, Integrated thermoeconomic optimization of standard

645   and regenerative ORC for different heat source types and capacities, Energy, 2017,

646   121:570-598.

647   [23] M. Mehrpooya, M. Ashouri, A. Mohammadi, Thermoeconomic analysis and

648   optimization of a regenerative two-stage organic Rankine cycle coupled with liquefied

649   natural gas and solar energy, Energy, 2017, 126:899-914.

650 [24] M. H. Yang, R. H. Yeh, Economic performances optimization of an organic

651 Rankine cycle system with lower global warming potential working fluids in

652 geothermal application, Renewable Energy, 2016, 85:1201-1213.

653 [25] M. Marion, I. Voicu, A. L. Tiffonnet, Study and optimization of a solar subcritical

654 organic Rankine cycle, Renewable Energy, 2012, 48(6):100-109.

655 [26] J. L. Wang, L. Zhao L, X. D. Wang, An experimental study on the recuperative

656 low temperature solar Rankine cycle using R245fa, Applied Energy, 2012,

657 94(2):34-40.

658 [27] H. Xi, M. J. Li, Y. L. He, W. Q. Tao, A graphical criterion for working fluid

659 selection and thermodynamic system comparison in waste heat recovery, Applied

660 Thermal Engineering, 2015, 89:772-782.

661 [28] P. J. Mago, L. M. Chamra, K. Srinivasan K, C. Somayaji, An examination of

662 regenerative organic Rankine cycles using dry fluids, Applied Thermal Engineering,

663 2008, 28(8):998-1007.

664 [29] C. Vetter, H. J. Wiemer, D. Kuhn, Comparison of sub- and supercritical Organic

665 Rankine Cycles for power generation from low-temperature/low-enthalpy geothermal

666 wells, considering specific net power output and efficiency, Applied Thermal

667 Engineering, 2013, 51(1–2):871-879.

668 [30] A. Javanshir, N. Sarunac, Thermodynamic analysis of a simple Organic Rankine

669 Cycle, Energy, 2017, 118:85-96.

670 [31] B. S. Dong, G. Q. Xu, X. Luo, L. H. Zhuang, Y. K. Quan, Analysis of the

671 Supercritical Organic Rankine Cycle and the Radial Turbine Design for High

Temperature Applications, Applied Thermal Engineering, 2017.

[32] B. S. Dong, G. Q. Xu, Y. Cai, H. W. Li, Analysis of zeotropic mixtures used in high-temperature Organic Rankine cycle, Energy Conversion and Management, 2014, 84:253-260.

[33] Z. Li, J. Bao, Thermodynamic analysis of organic Rankine cycle using zeotropic mixtures, Applied Energy, 2014, 130(8):748-756.

[34] J. Fischer, Comparison of trilateral cycles and organic Rankine cycles, Energy, 2011, 36(10):6208-6219.

[35] M. Yari, A. S. Mehr, V. Zare, S. M. S. Mahmoudi, M. A. Rosen, Exergoeconomic comparison of TLC (trilateral Rankine cycle), ORC (organic Rankine cycle) and Kalina cycle using a low grade heat source, Energy, 2015, 83:712-722.

[36] D. Fiaschi, G. Manfrida, F. Maraschiello, Design and performance prediction of radial ORC turboexpanders, Applied Energy, 2015, 138(C):517-532.

[37] J. Song, C. W. Gu, X. Ren, Parametric design and off-design analysis of organic Rankine cycle (ORC) system, Energy Conversion and Management, 2016, 112:157-165.

[38] E. Sauret, Y. Gu, Three-dimensional off-design numerical analysis of an organic Rankine cycle radial-inflow turbine, Applied Energy, 2014, 135(C):202-211.

[39] S. H. Kang, Design and preliminary tests of ORC (organic Rankine cycle) with two-stage radial turbine, Energy, 2016, 96:142-154.

[40] A. A. Jubori, R. K. Al-Dadah, S. Mahmoud, A.S. B. Ennil, K. Rahbar, Three dimensional optimization of small-scale axial turbine for low temperature heat source

694   driven organic Rankine cycle, Energy Conversion and Management, 2016,

695   133:411-426.

696   [41] J. Song, C. W. Gu, X. Ren, Influence of the radial-inflow turbine efficiency

697   prediction on the design and analysis of the Organic Rankine Cycle (ORC) system,

698   Energy Conversion and Management, 2016, 123:308-316.

699   [42] L. Pan, H. Wang, Improved analysis of Organic Rankine Cycle based on radial

700   flow turbine, Applied Thermal Engineering, 2013, 61(2):606-615.

701   [43] A. A. Jubori, A. Daabo, R. K. Al-Dadah, S. Mahmoud, A. B. Ennil, Development

702   of micro-scale axial and radial turbines for low-temperature heat source driven organic

703   Rankine cycle, Energy Conversion and Management, 2016, 130:141-155.

704   [44] K. Rahbar, S. Mahmoud, R. K. Al-Dadah, N. Moazami, Modelling and

705   optimization of organic Rankine cycle based on a small-scale radial inflow turbine,

706   Energy Conversion and Management, 2015, 91:186-198.

707   [45] A. J. Glassman, Computer program for design analysis of radial-inflow turbines,

708   1976.

709   [46] G. H. Ji, Turbine Expander, Machinery Industry Press, Beijing, 1989.

710   [47] C. A. M. Ventura, P. A. Jacobs, A. S. Rowlands, P. Petrie-repar, E. Sauret,

711   Preliminary design and performance estimation of radial inflow turbines: an automated

712   approach.

713   [48] A. M. A. Jubori, R. K. Al-Dadah, S. Mahmoud, A. Daabo, Modelling and

714   parametric analysis of small-scale axial and radial-outflow turbines for Organic

715   Rankine Cycle applications, Applied Energy, 2017, 190:981-996.

716   [49] R. Cauty, Genetic Algorithms and Engineering Optimization, Genetic algorithms

717   and engineering design, Wiley, 1997:379-381.

718   [50] E. Lemmon, M. Huber, M. McLinden, NIST Standard Reference Database 23,

719   NIST Reference Fluid Thermodynamic and Transport Properties–REFPROP, Version

720   9.0, Standard Reference Data Program, National Institute of Standards and Technology:

721   Gaithersburg, MD, 2010.

722   [51] Concepts NREC, 2012, http://www.conceptsnrec.com/.

723   [52] K. Rahbar, S. Mahmoud, R. K. Al-Dadah, N. Moazami, Parametric analysis and

724   optimization of a small-scale radial turbine for Organic Rankine Cycle, Energy, 2015,

725   83:696-711.

726

727

728

729

730

731

732

733

734

735

736

737

738 **Table and figure captions**

739 Fig.1. Schematic diagram of the basic ORC

740 Fig.2. Temperature-entropy curve of the basic ORC (using pentane)

741 Table 1 Working conditions for the heat source, heat sink and cycle parameters

742 Table 2 Properties of the working fluid candidates

743 Fig.3. h-s diagram of the radial-flow turbine

744 Fig.4. Velocity triangles of the radial-inflow turbine

745 Table 3 Recommended value ranges of the six optimized variables

746 Fig.5. Flowchart of the constrained GA

747 Table 4 Control operators of GA

748 Fig.6. Flowchart of the coupled ORC-turbine model

749 Table 5 Comparison of developed code with published codes

750 Fig.7. Variations of (a) pressure ratio and (b) mass flow rate with the outlet

751 temperature of the heat source

752 Fig.8. Variation of turbine efficiency with the outlet temperature of the heat source

753 Fig.9. Variations of the five kinds of losses with the outlet temperature of the heat

754 source using pentane and R123

755 Fig.10. Variation of cycle efficiency with the outlet temperature of the heat source

756 Fig.11. Variation of net power with the outlet temperature of the heat source

757 Fig.12. Variation of specific net power with the outlet temperature of the heat source

758 Fig.13. Variation of rotational speed (a), overall diameter (b) and Mach number at the

759 rotor inlet (c) with the outlet temperature of the heat source

760   Table 6 Optimized results of the preliminary design for the examined working fluids at

761   the maximum turbine efficiency condition